Materials Today Bio 32 (2025) 101649

Contents lists available at ScienceDirect

Materials Today Bio

journal homepage: www.journals.elsevier.com/materials-today-bio

Enhanced anticancer effect of carfilzomib by codelivery of calcium peroxide nanoparticles targeting endoplasmic reticulum stress

Dan Yin [a,1], Xuan Wu [a,1], Xu Chen [a], Jian-Li Chen [a], Xinyue Xia [b], Jianfang Wang [b], Xiuping Chen [c], Xiao-Ming Zhu [a,d,*]

[a] State Key Laboratory of Quality Research in Chinese Medicines & Faculty of Chinese Medicine, Macau University of Science and Technology, Taipa, Macau SAR, 999078, China
[b] Department of Physics, The Chinese University of Hong Kong, Shatin, Hong Kong SAR, 999077, China
[c] State Key Laboratory of Quality Research in Chinese Medicine, Institute of Chinese Medical Sciences, University of Macau, Taipa, Macau SAR, 999078, China
[d] Zhuhai MUST Science and Technology Research Institute, Macau University of Science and Technology, Zhuhai, Guangdong, 519099, China

ARTICLE INFO

Keywords:
Carfilzomib
Calcium peroxide
Proteasome inhibitors
Endoplasmic reticulum stress
Calcium overload

ABSTRACT

Encouraged by the clinical success of proteasome inhibitors treating hematological malignancy, continuous efforts are being made to improve their efficacy and expand their applications to solid tumor therapy. In this study, liposomes were used to encapsulate the proteasome inhibitor carfilzomib (CFZ) and calcium peroxide (CaO_2) nanoparticles for effective combination therapy targeting the interplay between calcium overload and oxidative stress. Low-dose CaO_2 synergistically enhances the anticancer effect of CFZ in the human glioblastoma U-87 MG cells. The reactive oxygen species (ROS) generation and glutathione depletion by low-dose CaO_2 complement CFZ-induced ubiquitinated protein accumulation further triggering endoplasmic reticulum (ER) stress leading to calcium overload and mitochondrial dysfunction. The liposome-based codelivery system is capable of transporting CFZ and CaO_2 simultaneously to the tumor, and results in a superior antitumor effect in U-87 MG tumor-bearing mice compared with monotherapy. Taken together, CaO_2 holds great potential to sensitize proteasome inhibitors in the treatment of solid tumors, and this work also presents a new combination therapy strategy targeting the crosstalk between proteasome inhibitors and oxidative stress for future cancer therapy.

1. Introduction

Ubiquitin-proteasome system (UPS) is the main intracellular route responsible for degrading damaged, unfolded and short-lived proteins [1]. It utilizes ubiquitin-activating enzyme (E1), ubiquitin-conjugating enzyme (E2) and ubiquitin ligase (E3) to link ubiquitin to substrate proteins to form polyubiquitin chains, which are ultimately recognized and degraded by the proteasome [2]. Proteasome inhibitors including bortezomib, carfilzomib (CFZ) and ixazomib have been developed clinically approved proteasome inhibitors for the treatment of multiple myeloma and mantle cell lymphoma [3]. As a representative second-generation proteasome inhibitor, the epoxyketone of CFZ irreversibly binds to proteasome subunits, prolonging the duration of proteasome inhibition [4]. Due to the poor aqueous solubility of CFZ, the current FDA-approved CFZ injection formulation contains sulfobutyl ether β-cyclodextrin as a solubilizer and stabilizer [5]. Encouraged by the clinical success of proteasome inhibitors treating hematological malignancy, continuous efforts have been made to expand their applications to solid tumor therapy, however, disappointing outcomes yielded in patients with solid tumors [5]. Moreover, side effects and acquired resistance also hamper the clinical applications of proteasome inhibitors [6]. In recent years, nanoparticle delivery systems such as liposomes [7], albumin nanocrystals [8] and lipid nanodiscs [9] have been developed to improve tumoral accumulation of CFZ through enhanced permeability and retention (EPR) effect, albeit without success in clinical translation.

As monotherapy with proteasome inhibitors for treating solid tumors shows inadequate efficacy, combination therapy with proteasome inhibitors and other therapies has been considered as an alternative strategy to broaden their applications [10,11]. Proteasome inhibition

* Corresponding author. State Key Laboratory of Quality Research in Chinese Medicines & Faculty of Chinese Medicine, Macau University of Science and Technology, Taipa, Macau SAR, 999078, China.
E-mail address: xmzhu@must.edu.mo (X.-M. Zhu).
[1] D. Yin and X. Wu contributed equally to this paper.

https://doi.org/10.1016/j.mtbio.2025.101649
Received 9 January 2025; Received in revised form 15 February 2025; Accepted 8 March 2025
Available online 10 March 2025

results in dramatic accumulation of ubiquitinated proteins which triggers endoplasmic reticulum (ER) stress by calcium overload leading to cell apoptosis [12]. Calium signaling pathways are mutually interconnected with reactive oxygen species (ROS) which cause oxidative damages to proteins, DNA, and lipids, ultimately inducing cell apoptosis [13]. Calcium overload characterized by excessive enrichment of intracellular Ca^{2+} can increase the production of ROS, and meanwhile ROS can affect calcium influx in to the cell and release from ER. Recently, oxidative stress inducing agents have been recognized as adjuvants for proteasome inhibitor therapy due to crosstalk between proteasome inhibitors and oxidative stress [14]. The cell-penetrating peptide GO-203 [15] and histone deacetylase (HDAC) inhibitors [16,17] were reported to sensitize the cancer cells to proteasome inhibitors by increasing intracellular ROS levels, highlighting a new strategy of the combination of ROS and proteasomal inhibition in cancer therapy. Moreover, the major antioxidant glutathione (GSH) presents in tumor microenvironment (TME) can react with ROS to resist oxidative stress thereby diminishing the efficacy of redox-targeted approaches [18,19]. It was reported that increasing intracellular GSH levels completely abolished the cytotoxicity of the first-generation proteasome inhibitor bortezomib [20]. Simultaneous enhancement of ROS generation and GSH depletion can be a promising strategy to improve the efficacy of proteasome inhibitors.

In recent years, metal peroxide nanoparticles (NPs) have received increasing attention in cancer therapy. Metal peroxide including calcium peroxide (CaO_2), BaO_2, CuO_2, ZnO_2 NPs can decompose to produce metal ions and hydrogen peroxide (H_2O_2) under the acidic conditions in TME, leading to metal ion overload and increased oxidative stress [21]. As one of the important second cellular messengers, calcium is involved in many intracellular signaling pathways. Regulation of calcium homeostasis may play a therapeutic role for treating some diseases. Therefore, among these metal oxide nanomaterials, CaO_2 has attracted the most attention in recent years [22,23]. In addition, CaO_2 has the advantages of facile synthesis and good biocompatibility. In the acidic TME and lysosomes, CaO_2 reacts with H^+ to generate Ca^{2+} ions and H_2O_2 [24,25]. Under the neutral condition, CaO_2 releases O_2 slowly. CaO_2 itself can induce calcium overload stress in cancer cells and subsequent apoptosis at high concentrations [26]. The multifunctional properties of CaO_2 also offer the potential for combinatorial cancer therapies. CaO_2 was reported to enhance the efficacies of photodynamic therapy [27,28], chemodynamic therapy [29], and immunotherapy [30]. Few studies have reported its synergistic effect with chemotherapy. So far, one study reported that calcium overload induced by CaO_2 sensitized the cancer cells to the anticancer drug doxorubicin [31].

Motivated by the excellent synergistic anticancer effect of oxidative stress and proteasome inhibitors, the CaO_2 NPs were incorporated with CFZ chemotherapy in this report. Considering that CaO_2 NPs are prone to react with water and decompose, liposomes co-loaded with CaO_2 NPs and CFZ (CFZ-CaO_2@Lip) were synthesized (Fig. 1). The distinctive core-shell nanostructure of liposomes enables them to encapsulate both hydrophobic and hydrophilic molecules. Hydrophobic CFZ can be loaded into the lipid bilayer of the liposomes, while CaO_2 NPs can be loaded into the inner cores of the liposomes during the film hydration process. Under the acidic condition, CaO_2 NPs decompose and produce Ca^{2+} and H_2O_2. In this study, the cytotoxic effect of CaO_2 NPs was found to be mainly attributed to the release of ROS rather than Ca^{2+}, especially at a low concentration. Low dosage of CaO_2 synergistically interacts with CFZ to induce dramatic ubiquitinated protein accumulation further triggering ER stress leading to calcium overload and mitochondrial dysfunction. Compared with the monotherapy with CFZ@Lip or

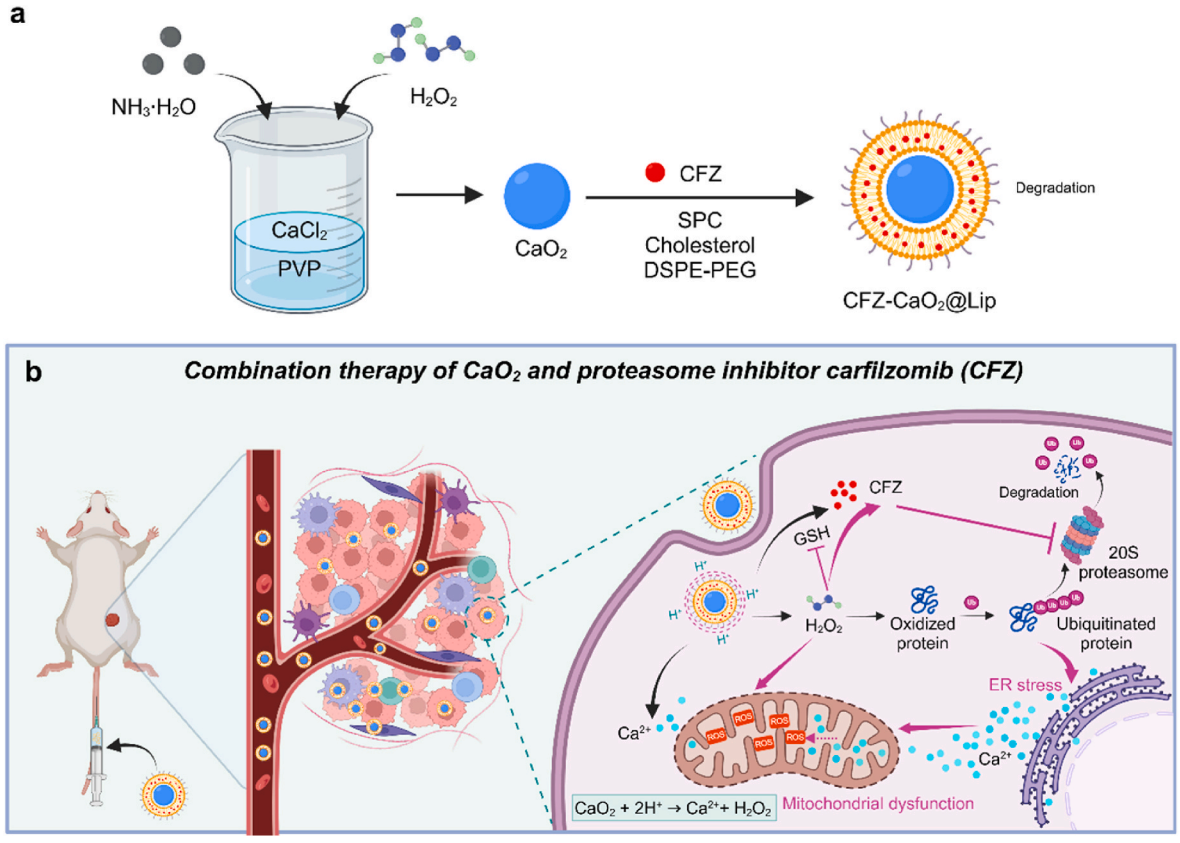

Fig. 1. Schematic illustration of codelivery of CaO_2 NPs and CFZ by liposomes. (a) Synthesis of CaO_2 NPs and preparation of liposomes co-loaded with CaO_2 NPs and CFZ (CFZ-CaO_2@Lip). (b) Under the acidic condition, CaO_2 decomposes and releases Ca^{2+} and H_2O_2. ROS generation and GSH depletion induced by CaO_2 at the low dosage synergistically enhance the cytotoxicity of CFZ. The combination therapy induces ubiquitinated protein accumulation triggering ER stress leading to calcium overload and mitochondrial injury and finally cell death.

CaO_2@Lip, the combination therapy with CFZ-CaO_2@Lip induces both stronger calcium overload and oxidative stress synergistically leading to apoptosis of human glioblastoma U-87 MG cells. This codelivery system enables simultaneous accumulation of both CFZ and CaO_2 in the tumors of U-87 MG tumor-bearing mice. The low-dose CaO_2 used in this study has no side effects on the liver and kidney, while it significantly improves the therapeutic efficacy of CFZ. Taken together, CaO_2 holds great potential in sensitizing the proteasome inhibitors for solid tumor therapy as they complement each other perfectly to induce synergistic calcium overload and oxidative stress.

2. Materials and methods

2.1. Chemicals and reagents

CFZ, JC-1 and DCFH-DA were purchased from MCE (USA). C6 was purchased from Sigma-Aldrich (USA). $CaCl_2$, ammonia ($NH_3{\cdot}H_2O$, 28−30 wt%), PVP 8000, glutathione, DTNB, NAC, DiR, MTT, oCPC, dimethyl sulfoxide (DMSO) and sodium citrate dihydrate were obtained from Aladdin (China). Soy lecithin (SPC) was purchased from AVT (China), cholesterol was purchased from Yuanye Biotechnology (China), and DSPE-PEG2000 was purchased from Xi'an Ruixi (China). H_2O_2 (30 wt%) was purchased from Xilong Scientific Co. Ltd (China). Fluo-4 AM, Alexa Fluor 555-conjugated and Alexa Fluor 488-conjugated goat anti-rabbit secondary antibody, Hoechst 33342, fetal bovine serum (FBS) and alpha-modified Minimum Essential Medium (α-MEM) were obtained from Thermo Fisher Scientific (USA). Ac-DEVD-AMC was purchased from Enzo Life Sciences (USA). Anti-PARP antibody (9542) was purchased from Cell Signaling Technology (USA). Antibodies (anti-β-actin (ab8226), anti-Ki67 (ab15580)) and BAPTA-AM were obtained from Abcam (UK). Antibodies (anti-ubiquitin (sc-8017), goat anti-mouse IgG-HRP (sc-2005) and goat anti-rabbit IgG-HRP (sc-2004)) were purchased from Santa Cruz (USA). Precision Plus Protein Dual Color was obtained from Bio-Rad Laboratories (USA). Hilymax was purchased from Dojindo Laboratories (Japan). TUNEL apoptosis assay kit was obtained from Beyotime (China). FITC Annexin V apoptosis detection kit was obtained from BD Biosciences (USA). GSH, AST, ALT, BUN and CRE assay kits were purchased from Nanjing Jiancheng Bioengineering Institute (China). Human glioblastoma U-87 MG cells were purchased from American Type Culture Collection (ATCC, USA).

2.2. Synthesis of CaO_2 NPs

CaO_2 NPs were synthesized by a one-step method at room temperature. In brief, $CaCl_2$ (40 mg) and PVP 8000 (120 mg) were dissolved completely in ethanol (8 mL). The solution was stirred vigorously for 30 min, $NH_3{\cdot}H_2O$ (0.8 M, 400 μL) was then injected into the system to activate the reaction, followed by adding H_2O_2 (40 μL). After further stirring for 2 h, the mixed solution was centrifuged at 12000 rpm for 20 min, and the obtained pellet product was washed twice with ethanol and finally dispersed in ethanol.

2.3. Synthesis of CaO_2@Lip

SPC (8.3 mg), cholesterol (1.6 mg), and DSPE-PEG2000 (4 mg) were mixed and dissolved in chloroform (10 mL). CaO_2 NPs (12 mg mL^{-1},100 μL, dispersed in ethanol) were then added. The mixture was dried under reduced pressure at 30 °C by a rotary evaporator to form a lipid film. The film was hydrated by adding water and then sonicated (480 W, 8 kHz, 1 s on and 1 s off) in an ice bath for 5 min before obtaining CaO_2@Lip.

2.4. Characterization of CaO_2@Lip

The sizes of CaO_2 NPs and CaO_2@Lip were measured by dynamic light scattering using Malvern Zetasizer Nano ZS90 analyzer. The morphology and mapping analysis were observed by TEM and EDX by using FEI HRTEM TF20.

2.5. Calcium content assay

The calcium content was detected by the oCPC method. HCl was used to dissolve the CaO_2@Lip, followed by ultrasonication for 10 min. The diluted sample (50 μL) was added to oCPC solution (0.1 mg mL^{-1} in Tris HCl buffer, pH = 11.7, 150 μL), and the obtained mixture was incubated for 5 min protected from light. The absorbance at 575 nm was measured by a SpectraMax Paradigm multimode microplate reader (Molecular Devices, USA).

2.6. GSH depletion by CaO_2@Lip

The GSH assay was performed based on the reaction between GSH and DTNB. In brief, GSH (0−250 μM, 60 μL) was incubated with DTNB solution (0.1 mM in Tris HCl buffer, pH = 8.3, 120 μL) for 5 min, and the absorbance at 230−560 nm was measured by the microplate reader. This assay was then used to detect GSH depletion by CaO_2@Lip. CaO_2@Lip (0−125 μg mL^{-1}, 390 μL) was mixed with GSH (10 mM, 10 μL) and incubated at 37 °C for 1 h, followed by centrifugation at 9000 rpm for 10 min. The supernatant (60 μL) was incubated with DTNB solution for 5 min, and the absorbance at 230−560 nm was measured by the microplate reader.

2.7. CFZ loading

The CFZ-CaO_2@Lip was prepared according to a similar procedure of CaO_2@Lip by adding CFZ into chloroform, while CFZ@Lip was prepared without adding CaO_2 NPs. The products were centrifuged with an ultrafiltration tube (molecular weight cut-off: 300 kDa) at 4000 rpm for 20 min to remove free CFZ, CFZ-CaO_2@Lip was obtained from the upper layer in the ultrafiltration tube.

For the drug encapsulation and loading efficiency study, ten times the volume of methanol was added to CFZ-CaO_2@Lip to break the emulsification, followed by 10-min ultrasonication. After centrifugation (12000 rpm, 30 min), the CFZ concentration of the supernatant was detected by an Agilent 6230 time-of-flight liquid chromatography-mass spectrometry (LC-MS) system (USA). The CFZ encapsulation efficiency (EE) and loading content (LE) were calculated using the following equations:

$$\text{EE (\%)} = (\text{mass of CFZ in the CFZ-}CaO_2\text{@Lip/total mass of CFZ added}) \times 100\ \% \quad (1)$$

$$\text{LE (\%)} = (\text{mass of CFZ in the CFZ-}CaO_2\text{@Lip/total mass of CFZ-}CaO_2\text{@Lip}) \times 100\ \% \quad (2)$$

2.8. CFZ desorption assay

The release of CFZ from CFZ-CaO_2@Lip was carried out by a dialysis method. The above obtained CFZ-CaO_2@Lip (0.4 mg, 1 mL) was transferred into a dialysis bag and placed in a beaker containing 40 mL of PBS or citrate buffer (20 mM, pH 4.5), followed by stirring 0−48 h at 100 rpm at 37 °C. The portion (500 μL) of the release solution was taken at different time points, and the same volume of PBS or citrate buffer was supplemented to the solution. After centrifugation (12000 rpm, 30 min), the drug concentration of the supernatant was detected by the LC-MS system.

2.9. Cell culture

U-87 MG cells were cultured in α-MEM containing 10 % FBS, streptomycin (100 μg mL^{-1}) and penicillin (100 U mL^{-1}) in a humidified incubator at 37 °C and 5 % CO_2 atmosphere. GFP-ubiquitin plasmid was

transfected into U-87 MG cells by using Hilymax, and the U-87 MG cells stably expressing GFP-ubiquitin were maintained in α-MEM with geneticin (500 μg mL^{-1}).

2.10. Cellular uptake assay

The CaO_2@Lip was first loaded with the fluorescent probe C6. Five thousand U-87 MG cells per well were seeded into a 96-well plate and then treated with different concentrations of C6-loaded CaO_2@Lip (C6/CaO_2@Lip). After 6-h incubation, PBS was used to wash the CaO_2@Lip adsorbed on the surface of the cells. The cells were then stained with Hoechst 33342 (100 ng mL^{-1}) for 15 min. The fluorescence imaging was performed on an Olympus IX71 fluorescence microscope (USA) to study the intracellular distribution of CaO_2@Lip.

For flow cytometry analysis, 1.5×10^5 U-87 MG cells per well were seeded into a 6-well plate and then treated with different concentrations of C6/CaO_2@Lip. After 6-h incubation, the cells were finally trypsinized and the flow cytometry analysis was carried out on a BD FACSAria III system (USA).

2.11. Imaging of GFP-ubiquitin puncta

Three thousand U-87 MG cells stably expressing GFP-ubiquitin per well were seeded into a 96-well plate and treated with CaO_2@Lip (20 μg mL^{-1} CaO_2), CFZ@Lip (10 nM CFZ), or CFZ-CaO_2@Lip (10 nM CFZ, 20 μg mL^{-1} CaO_2) for 24 h. The intracellular GFP-ubiquitin puncta were observed under the fluorescence microscope.

2.12. Western blotting assay

After the treatment, the cells were collected, washed twice with PBS and lysed with RIPA buffer at 4 °C for 1 h, during which time the cells were vortexed every 15 min. After centrifugation at 4 °C (12000 rpm, 15 min), the total proteins were obtained. Bradford protein assay was used to determine the protein concentration, and 30 μg of the protein samples were then separated and transferred to a PVDF membrane. Afterwards, the PVDF membrane was blocked with 5 % nonfat milk for 1 h, followed by incubation with primary antibodies on a shaker at 4 °C at a slow speed overnight. Then the PVDF membrane was subsequently incubated with corresponding secondary antibodies for 1 h at room temperature and visualized using enhanced chemiluminescence (ECL) reagents.

2.13. JC-1, Fluo-4 AM, and DCFH-DA staining

Five thousand U-87 MG cells were seeded into in a 96-well plate and incubated overnight. The cells were then treated with CaO_2@Lip (20 μg mL^{-1} CaO_2), CFZ@Lip (10 nM CFZ), or CFZ-CaO_2@Lip (10 nM CFZ, 20 μg mL^{-1} CaO_2). After 8-h incubation, the cells were washed with PBS twice and stained with fresh FBS-free medium containing DCFH-DA (10 μM) for 20 min to stain intracellular reactive oxygen species (ROS). For calcium and mitochondrial membrane potential detection, after 24-h incubation, the cells were stained with JC-1 (4 μM) or Fluo-4 AM (0.5 μM) for 20 min, respectively. Afterwards, the cells were stained with Hoechst 33342 (100 ng mL^{-1}) for 15 min. The cells were washed twice with PBS and observed by a fluorescence microscope.

2.14. Cell viability assay

Three thousand U-87 MG cells per well were seeded into a 96-well plate, and after incubation for 12 h, the cells were treated with different concentrations of CaO_2@Lip in the presence or absence of tool inhibitor (2 mM NAC or 4 μM BAPTA-AM) for 48 h. The medium was changed with a fresh medium containing MTT (0.5 mg mL^{-1}). After 3-h incubation, the medium was discarded and DMSO (150 μL) was added to dissolve the purple formazan crystals. After shaking for 10 min, the absorbance at 540 nm of the solution was detected by the microplate reader.

2.15. Synergistic cytotoxicity of CFZ-CaO_2@Lip

Three thousand U-87 MG cells per well were seeded into a 96-well plate and treated with CFZ@Lip (0−40 nM CFZ), CaO_2@Lip (20 μg mL^{-1} CaO_2), or CFZ-CaO_2@Lip (0−40 nM CFZ, 20 μg mL^{-1} CaO_2) in the presence or absence of NAC (2 mM) for 48 h. The cell viability was detected by the MTT assay.

Effect of combination treatment of CFZ and $CaCl_2$ on cell viability.

Three thousand U-87 MG cells per well were seeded into a 96-well plate and treated with CFZ (0−40 nM) in the presence or absence of $CaCl_2$. The concentration of $CaCl_2$ was 277 μM, which was equivalent to the concentration of calcium ion in CaO_2@Lip (20 μg mL^{-1} CaO_2). The cell viability was detected by the MTT assay.

2.16. Cell apoptosis assay

Seventy thousand U-87 MG cells per well were seeded into a 6-well plate. After overnight incubation, the cells were treated with CaO_2@-Lip (20 μg mL^{-1} CaO_2), CFZ@Lip (20 nM CFZ), or CFZ-CaO_2@Lip (20 nM CFZ, 20 μg mL^{-1} CaO_2). After 24-h incubation, both the medium and cells were collected and stained with FITC Annexin V apoptosis detection kit, and flow cytometry analysis was performed on a BD FACSAria III system.

2.17. Intracellular GSH content assay

Seventy thousand U-87 MG cells per well were seeded into a 6-well plate. After overnight incubation, the cells were treated with CaO_2@-Lip (20 μg mL^{-1} CaO_2), CFZ@Lip (20 nM CFZ), or CFZ-CaO_2@Lip (20 nM CFZ, 20 μg mL^{-1} CaO_2). After 24-h incubation, the cells were lysed with RIPA buffer at 4 °C for 30 min to obtain total proteins, and the protein concentration was detected by Bradford protein assay. The intracellular GSH content was detected by a GSH assay kit according to the manufacturer's instruction.

2.18. Caspase-3 activity assay

After the treatments, the cells were washed twice with PBS and lysed with a lysis HEPES buffer (HEPES (50 mM), NP-40 (0.5 %), ATP (1 mM), KCl (1.5 mM), sucrose (250 mM), NaCl (10 mM), EDTA (1 mM), dithiothreitol (1 mM), pH 7.4) at 4 °C for 1 h, and the cells were vortexed every 15 min. After centrifugation (12000 rpm, 15 min) at 4 °C, the total proteins were obtained. 15 μg of total protein were added to the above HEPES buffer (without NP-40, 100 μL) containing the caspase-3 substrate Ac-DEVD-AMC (10 μg mL^{-1}). After 30-min incubation at 37 °C protected from light, the fluorescence intensity with excitation at 355 nm and emission at 460 nm was measured by the microplate reader.

2.19. Animals

BALB/c nude mice (female, 6−8 weeks of age) were used in the animal experiments in this work. All animal experiments were conducted in compliance with Institutional Guide for Care and Use of Laboratory Animals from the animal ethics committee (Macau University of Science and Technology).

2.20. In vivo biocompatibility study

The BALB/c nude mice were intravenously injected with the CaO_2@Lip (20 mg kg^{-1} CaO_2) and sacrificed after 14 days. The major organs of the mice, including heart, liver, spleen, lung and kidney, were harvested and fixed with 4 % paraformaldehyde (PFA), embedded in paraffin, sectioned, and stained with hematoxylin and eosin (H&E). The images were observed by a Leica DM2500 fluorescence microscope

(Germany). The plasma of the mice was collected to detect the activities of liver aminotransferases (AST and ALT) and the levels of kidney function indicators (BUN and CRE).

2.21. Tumor xenograft

The BALB/c nude mice were subcutaneously implanted with 1×10^7 U-87 MG cells suspended in PBS (100 μL) into the backside flank to establish the tumor model. The tumor sizes were measured using a caliper. The tumor volumes were calculated based on the equation (tumor length) × (tumor width)^2/2.

2.22. In vivo biodistribution of CaO_2@Lip

The CaO_2@Lip was loaded with the fluorescent dye DiR. The U-87 MG-tumor bearing mice were injected with the DiR-loaded CaO_2@Lip (20 mg kg^{-1} CaO_2, 200 μg kg^{-1} DiR) via the tail vein. After 6 or 12 h, the mice were sacrificed and *ex vivo* imaging of the major organs and tumors were carried out on an IVIS imaging system (AniView100, BLT, China).

2.23. In vivo antitumor study

When the tumor volumes of the U-87 MG-tumor bearing mice reached approximately 100 mm^3, the day was defined as day 0. The mice were randomly divided into four groups (n = 5), and intravenously injected with (1) saline (control group), (2) CaO_2@Lip (20 mg kg^{-1} CaO_2), (3) CFZ@Lip (2 mg kg^{-1} CFZ), or (4) CFZ-CaO_2@Lip (20 mg kg^{-1} CaO_2, 2 mg kg^{-1} CFZ). The injection was performed on day 0, 2, 4, 8. The tumor sizes were measured with a caliper every other day for 14 days. All mice were sacrificed on day 14, and the tumor tissues were harvested, fixed, embedded, sectioned, and stained with H&E. Proteins of the tumors were collected for the western blotting assay and GSH content detection.

The tumor tissues were also fixed with PFA overnight, and then dehydrated with gradient sucrose solution. Frozen sections (5 μm) were obtained using a Leica CM3050S cryostat (Germany). For the detection of the expression of Ki67 and ubiquitinated proteins, the tumor slices were permeabilized with 0.1 % Triton X-100, blocked with 10 % goat serum, and incubated with anti-Ki67 and anti-ubiquitin primary antibody in a shaker at 4 °C overnight. The tumor slices were then incubated with Alexa Fluor 488 conjugated goat anti-rabbit secondary antibody for 1 h and stained with Hoechst 33342 (10 μg mL^{-1}) for 30 min at room temperature. For DCFH-DA staining, the tumor slices were incubated with DCFH-DA (10 μM) for 30 min and Hoechst 33342 for 30 min. For the TUNEL analysis, the tumor slices were permeabilized and incubated with TUNEL test solution for 1 h and Hoechst 33342 for 30 min. The fluorescence images of the samples were captured by a Zeiss Axio Observer Z1 fluorescence microscope (Germany).

2.24. Statistical analysis

All experiments were carried out at least three times and the results were presented as mean ± standard errors of the mean (S.E.M.). Statistical analysis was performed by using GraphPad Prism 8 (GraphPad Software Inc. USA). The statistical differences were evaluated using one-way analysis of variance (ANOVA) followed by Tukey's post hoc test. A $P < 0.05$ was considered as statistically significant.

3. Results and discussion

3.1. Synthesis and characterization of CaO_2@Lip

CaO_2 NPs were first synthesized at room temperature. In brief, the reaction was carried out by mixing calcium chloride ($CaCl_2$), polyvinylpyrrolidone 8000 (PVP 8000), ammonia solution ($NH_3 \cdot H_2O$) and H_2O_2 in an ethanol system and stirring for 2 h. The CaO_2 NPs were obtained after centrifugation and dispersed in ethanol. The CaO_2 NPs obtained exhibit a relatively uniform size as determined from the transmission electron microscopy (TEM) imaging (Fig. 2a). The composition of the CaO_2 NPs was determined by energy-dispersive X-ray spectroscopy (EDX). Fig. 2b shows that Ca and O elements are distributed in the NPs, indicating that the NPs are CaO_2. As the dynamic light scattering result shown in Fig. 2c, the hydrodynamic size of CaO_2 is 54.6 ± 2.1 nm.

CaO_2@Lip was prepared by a film dispersion method. SPC, cholesterol, DSPE-PEG2000 dissolved in chloroform and CaO_2 NPs dissolved in ethanol were dried to form a lipid film using a rotary evaporator. Subsequently, water was added to hydrate the membrane, resulting in the formation of CaO_2@Lip. The TEM image of CaO_2@Lip was displayed in Fig. 2d, and the hydrodynamic size was determined to be 141.2 ± 8.9 nm (Fig. 2e).

In the acidic TME and lysosomes, CaO_2 reacts with H^+ to generate Ca^{2+} ions and H_2O_2 [32]. The concentration of Ca^{2+} was measured by an o-cresolphthalein complexone (oCPC) method (Fig. S1). For the determination of the GSH consumption capacity of CaO_2@Lip due to the released H_2O_2, a GSH assay was performed based on the oxidation of GSH by 5,5′-dithiobis-(2-nitrobenzoic acid) (DTNB, with an absorption peak at 325 nm) to form the yellow derivative 5-thio-2-nitrobenzoic acid (TNB, with an absorption peak at 412 nm). The initial GSH concentration can be measured according to UV–vis absorption spectrum. As shown in Fig. 2f, the absorbance at 412 nm is proportional to the GSH concentration added to the reaction solution, indicating that GSH quantification is reasonable. Correspondingly, under the same GSH content, the CaO_2@Lip amount is inversely related to the TNB produced, suggesting the GSH depletion ability of CaO_2@Lip by self-supplying H_2O_2 (Fig. 2g). This result indicates that CaO_2@Lip can affect cellular redox balance by consuming intracellular GSH.

3.2. CFZ loading and release

As an irreversible second-generation proteasome inhibitor, CFZ establishes a covalent link through its epoxy ketone interaction with the N-terminal threonine of the proteasome active site, and mainly inhibits chymotrypsin-like (β5) activity [33]. However, CFZ exhibits a low solubility in aqueous solutions, necessitating the use of drug delivery systems to address this issue. Nanoparticle delivery system is considered as a preferred option due to their high loading capacity and ability to target tumors [34].

As self-assembled bilayer spheres made of amphiphilic molecules, liposomes are ideal drug carriers for both hydrophobic and hydrophilic drugs [35]. Liposomes were thus utilized to co-load CaO_2 and CFZ to obtain CFZ-CaO_2@Lip. The CFZ concentration was determined using LC-MS analysis (Fig. S2). The loading capacity and encapsulation efficiency of CFZ in CFZ-CaO_2@Lip were determined to be 12.4 wt% and (77.4 ± 5.3)%, respectively (Fig. 3a). Besides, the hydrodynamic size of CFZ-CaO_2@Lip is approximately 150 nm, which is slightly increased compared with CaO_2@Lip (Fig. 3b). NPs, including liposomes, generally enter cells via endocytosis and are then largely transported into acidic endosomes and lysosomes [36,37]. Phosphate buffered saline (PBS) and citrate buffer (lysosome/endosome mimicking buffer, pH 4.5) were used to study the CFZ release behavior [38,39]. As shown in Fig. 3c, CFZ release of CFZ-CaO_2@Lip is pH-dependent. After incubation using a dialysis bag for 48 h, the release amount of CFZ in citrate buffer is (80.9 ± 4.5)%, while that in PBS is only (46.6 ± 5.0)%.

3.3. Synergistic cellular disorder induced by CFZ-CaO_2@Lip in U-87 MG cells

The UPS eliminates damaged, misfolded, or unnecessary proteins from cells to control cellular functions. This process involves two stages: ubiquitination of target proteins and their degradation by the proteasome [40]. Ubiquitin is a 76-amino-acid protein that initially binds to

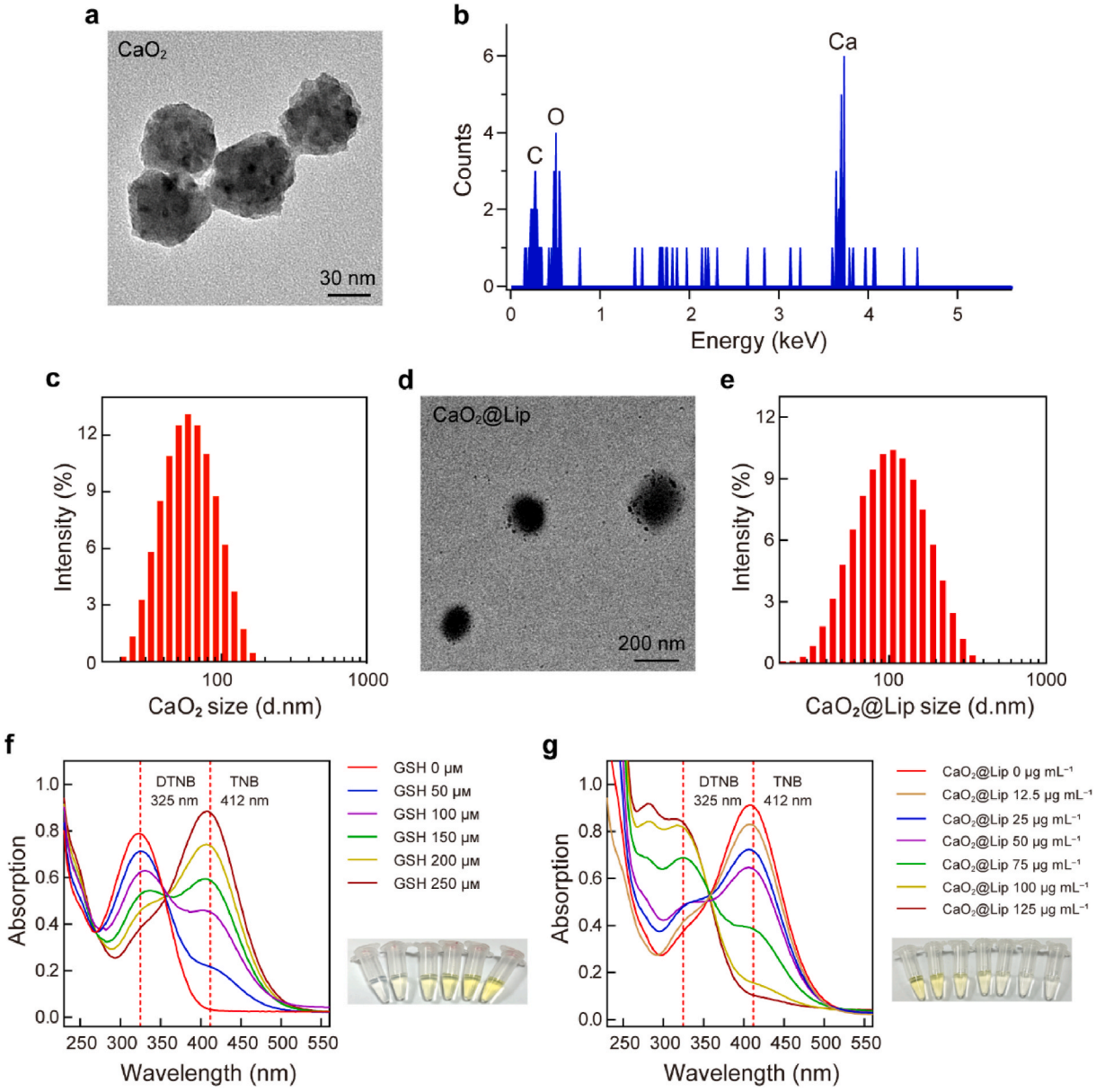

Fig. 2. Characterization of CaO_2@Lip. (a) TEM image of CaO_2 NPs. (b) EDX spectrum profile of CaO_2 NPs. (c) Hydrodynamic size of CaO_2 NPs. (d) TEM image of CaO_2@Lip. (e) Hydrodynamic size of CaO_2@Lip. (f) UV–vis absorbance spectra of DTNB solutions after reaction of various concentrations of GSH. (g) UV–vis absorbance spectra of DTNB solutions after reaction of GSH (250 μM) in the presence of various concentrations of CaO_2@Lip.

the target protein, guaranteeing accurate recognition by the proteasome for degradation [40]. Polyubiquitination is a process facilitated by a series of enzymes (E1, E2, and E3) that sequentially deliver ubiquitin molecules to target proteins [41]. The proteasome complex recognizes ubiquitinated proteins, deubiquitinates, unfolds, and cleaves them into peptide products, and the ubiquitin chains are recycled [41]. Herein the effect of CFZ-CaO_2@Lip on UPS was evaluated.

Human glioblastoma U-87 MG cells were used in this study. The fluorescent probe coumarin 6 (C6) was used to label CaO_2@Lip to study their uptake profile in the U-87 MG cells. Both fluorescence imaging and flow cytometry analysis demonstrate that CaO_2@Lip can be taken up by the cells in a dose-dependent manner (Fig. S3). U-87 MG cells stably expressing green fluorescent protein-tagged ubiquitin (GFP-ubiquitin) were used to study the intracellular levels of ubiquitinated proteins after the treatments. The effect of CFZ-CaO_2@Lip on UPS was compared with the monotherapy with CFZ @Lip or CaO_2@Lip. As expected, CFZ@Lip (10 nM CFZ) alone induces accumulation of GFP-ubiquitin puncta (Fig. 4a) and enhances the expression of ubiquitinated proteins (Fig. 4b). Even if CaO_2@Lip (20 μg mL^{-1} CaO_2) has little effect on UPS, treatment with CFZ-CaO_2@Lip results in dramatic accumulation of GFP-ubiquitin puncta (Fig. 4a) and ubiquitinated proteins (Fig. 4b), as compared with the monotherapy.

Mitochondria, being the "powerhouse" of cells, are crucial for supplying significant energy to tumor cells [42]. Importantly, mitochondria are also involved in various fundamental cell functions such as calcium homeostasis, ROS regulation, ATP production, and apoptosis [43]. The potential-dependent fluorescent probe JC-1 was utilized for detecting mitochondrial membrane potential (MMP). JC-1 forms aggregates in the normal mitochondrial matrix and emits intense red fluorescence, whereas it is unable to form aggregates and emits green fluorescence when the mitochondrial membrane potential is lowered. As shown in Fig. 4c, compared with the control group, the red fluorescence signal in the group of CaO_2@Lip (20 μg mL^{-1} CaO_2) or CFZ@Lip (10 nM CFZ) is weaker, while the green fluorescence intensity is stronger. Compared

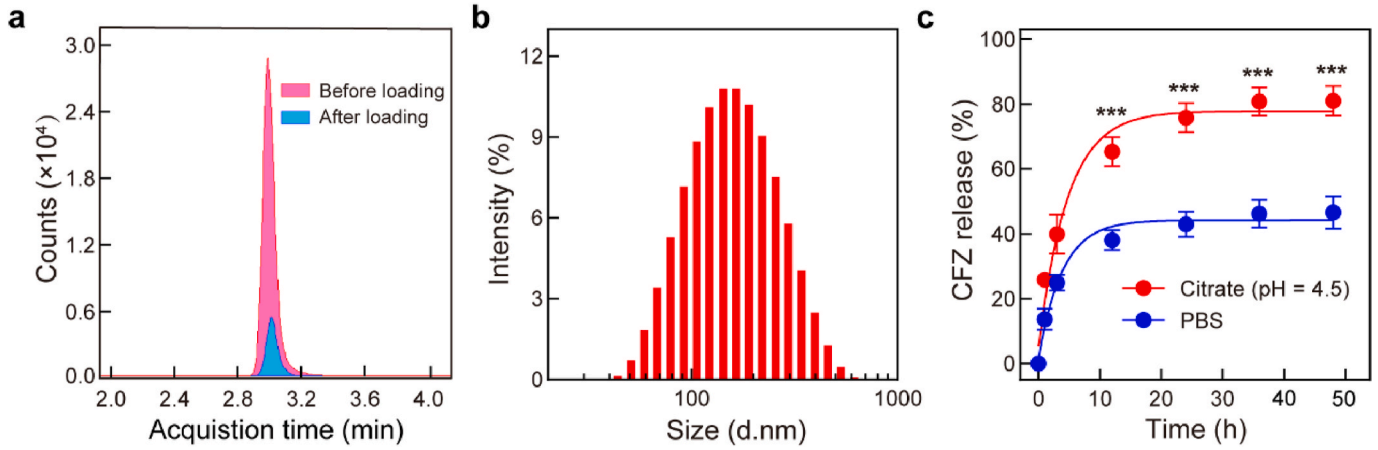

Fig. 3. Loading and release of CFZ from CFZ-CaO_2@Lip. (a) LC-MS chromatograms of CFZ for the initial solution and the filtrate after drug loading. (b) Hydrodynamic size of CFZ-CaO_2@Lip. (c) CFZ release profile of the CFZ-CaO_2@Lip in PBS or citrate buffer (20 mM, pH 4.5) at 37 °C. The data shown represent the mean ± S.E.M., $n = 3$, $^{***}P < 0.001$.

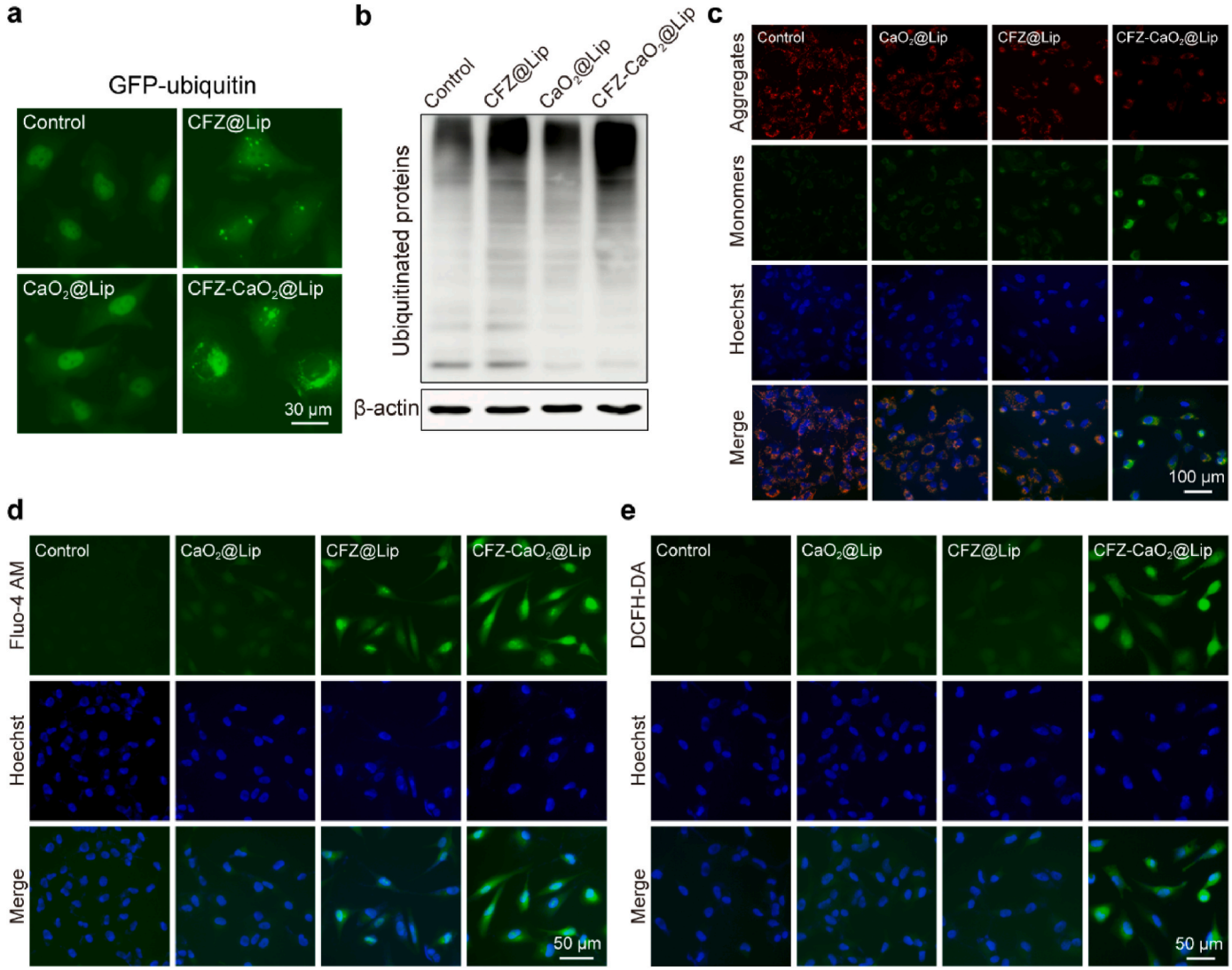

Fig. 4. Synergistic cellular disorder induced by CFZ-CaO_2@Lip in U-87 MG cells. (a) Imaging of GFP-ubiquitin puncta and (b) western blotting analysis of the expression of ubiquitinated proteins in the U-87 MG cells. (c) JC-1, (d) Ca^{2+}, and (e) ROS staining of the cells. After the treatment, the cells were stained with JC-1 (4 μM, green and red), Fluo-4 (0.5 μM, green), and DCFH-DA (10 μM, green) to study the cellular MMP, Ca^{2+} content, and ROS level, respectively. Cell nuclei were stained with Hoechst 33342 (100 ng mL^{-1}, blue). The cells were treated with CFZ@Lip (10 nM CFZ), CaO_2@Lip (20 μg mL^{-1} CaO_2), or CFZ-CaO_2@Lip (10 nM CFZ, 20 μg mL^{-1} CaO_2) for 24 h. (For interpretation of the references to colour in this figure legend, the reader is referred to the Web version of this article.)

either mono-treatment, CFZ-CaO_2@Lip further reduces the red fluorescence and enhance the green fluorescence intensity, indicating that the combination treatment with CFZ-CaO_2@Lip induces a lowest mitochondrial membrane potential (Fig. 4c). This phenomenon may be due to excessive Ca^{2+} released from CaO_2 NPs and induced from CFZ, resulting in mitochondrial signaling disorders, which is beneficial to anticancer therapy [44]. Moreover, proteasome plays a vital role in shaping mitochondria, the inhibition of UPS triggers not only the accumulation of ubiquitinated proteins, but also mitochondrial dysfunction [45].

A cell-permeable green-fluorescent Ca^{2+} indicator Fluo-4 AM was utilized for detecting intracellular Ca^{2+}. CaO_2@Lip induces a higher level of intracellular Ca^{2+} in a dose-dependent manner (Fig. S4). Significant higher intracellular Ca^{2+} level was observed after the cells were treated with CFZ@Lip (10 nM CFZ) (Fig. 4d), and this phenomenon is attributed to the efflux of Ca^{2+} from the ER into the cytoplasm under ER stress caused by CFZ, thereby leading to the increased concentration of Ca^{2+} [46]. Importantly, CaO_2@Lip (20 μg mL^{-1} CaO_2) cooperates with CFZ@Lip (10 nM CFZ) to further elevate intracellular Ca^{2+} content (Fig. 4d). As expected, the combination of CaO_2@Lip and CFZ@Lip synergistically enhance the ROS level (Fig. 4e).

It has been reported that several proteasome inhibitors like bortezomib, MG-132 and have been shown to elevate intracellular levels of ROS [47–49]. A fluorescence probe 2′,7′-dichlorodihydrofluorescein diacetate (DCFH-DA) was also used to detect intracellular ROS. CaO_2@Lip also enhances the intracellular ROS level in a dose-dependent (Fig. S5). Compared with control group, CaO_2@Lip (20 μg mL^{-1} CaO_2) or CFZ@Lip (10 nM CFZ) mildly elevates the ROS level, however, the combination treatment with CFZ-CaO_2@Lip (10 nM CFZ, 20 μg mL^{-1} CaO_2) synergistically induces a dramatic intracellular ROS level (Fig. 4e).

3.4. Synergistic cytotoxicity induced by CFZ-CaO_2@Lip in U-87 MG cells

Even though CFZ has been approved for many years, its efficacy in solid tumors is unsatisfactory. In view of the fact that the combination of CaO_2 and CFZ can lead to homeostasis disorder of cells, the cytotoxic effect of CFZ-CaO_2@Lip was then studied in the U-87 MG cells.

Cell viability was determined by the 3-(4,5-dimethylthiazol-2-yl)-2,5-diphenyltetrazolium bromide (MTT) assay. As shown in Fig. 5a, CaO_2@Lip inhibits the cell viability dose-dependently. In order to identify the cytotoxic effect of CaO_2@Lip was caused by excess released Ca^{2+} or ROS, the cells were treated with CaO_2@Lip in the presence or absence of a Ca^{2+} chelator 1,2-bis(2-aminophenoxy)ethane-N,N,N′,N′-tetraacetic acid tetrakis (acetoxymethyl ester) (BAPTA-AM) or an antioxidant N-acetylneuraminic acid (NAC). The result indicates that BAPTA-AM does not affect the cytotoxicity of low concentrations of CaO_2@Lip (20−40 μg mL^{-1} CaO_2), whereas NAC greatly reverses the cell viability (Fig. 5b and c), suggesting that the cytotoxicity effect of CaO_2@Lip at the low concentration is primarily attributed to the released ROS, rather than Ca^{2+}. However, at the high CaO_2 concentration of 80 μg mL^{-1}, both Ca^{2+} and ROS contribute to the cytotoxicity of CaO_2@Lip (Fig. 5b and c). Zhang et al. also reported that CaO_2 induced cytotoxicity at the high CaO_2 concentration of 60 μg mL^{-1} was attributed to calcium overload [26]. Therefore, whether CaO_2 induces oxidative stress or calcium overload is dependent on its dosage. As the close interrelationship between calcium and ROS, the induced increases of calcium overload and ROS are believed to create a self-amplifying loop in the cells [13,50]. Because CaO_2@Lip at the low CaO_2 concentration of 20 μg mL^{-1} can increase both calcium and ROS (Fig. 4d and e), the induced mild increase of calcium may contribute to the ROS elevation.

CaO_2@Lip (20 μg mL^{-1} CaO_2) which induces the cell viability to be (71.2 ± 1.3)% was chosen for the combination therapy of CaO_2 and CFZ. CaO_2@Lip (20 μg mL^{-1} CaO_2) synergistically enhances the cytotoxicity of CFZ at varying concentrations. The viability of the cells treated with CFZ@Lip (20 nM CFZ) is (68.5 ± 2.8)%, while CFZ-CaO_2@Lip dramatically reduces the cytotoxicity to (37.4 ± 1.3)% (Fig. 5d). In several previous reports, calcium overload can enhance the cytotoxic effect of chemotherapeutic agents [31,51]. Therefore, further studies were performed to distinguish the roles of Ca^{2+} and ROS involved in the synergistic effect. We found that $CaCl_2$ (277 μM) containing the same amount of Ca^{2+} as CaO_2@Lip (20 μg mL^{-1} CaO_2) does not affect the viability of the cells treated with CFZ@Lip (Fig. S6), further indicating that the synergistic cytotoxicity of CFZ@Lip is attributed to ROS generated by CaO_2@Lip. As expected, NAC reverses the toxicity of CFZ-CaO_2@Lip to a similar level as CFZ@Lip (Fig. 5e). Moreover, lowest intracellular GSH content was detected after the cells were treated with CFZ-CaO_2@Lip (Fig. 5f).

A flow cytometry assay was conducted using AnnexinV-FITC and PI staining to evaluate cell apoptosis. The apoptosis rates in CaO_2@Lip (20 μg mL^{-1} CaO_2) and CFZ@Lip (20 nM CFZ) groups are (21.5 ± 1.7)% and (30.3 ± 1.5)%, respectively. Importantly, treatment of CFZ-CaO_2@Lip enhances the apoptosis rate to (61.9 ± 0.7)% (Fig. 5g, Fig. S7), which was consistent with the MTT result. Caspase-3 is a crucial cysteine protease that plays a key role in the apoptosis process. It functions by cleaving various apoptosis-related proteins, such as poly (ADP-ribose) polymerase (PARP), which is a DNA repair enzyme. During apoptosis, caspase-3 cleaves PARP, leading to its inactivation and facilitating apoptosis progression [52]. A selective fluorescent substrate Ac-DEVD-AMC was used to determine the caspase-3 activity. As compared with control group, the caspase-3 activity for the cells treated with CaO_2@Lip (20 μg mL^{-1} CaO_2) and CFZ@Lip (20 nM CFZ) are (131.3 ± 12.4)% and (138.9 ± 4.4)%, respectively. The CFZ-CaO_2@Lip enhances the caspase-3 activity to (204.8 ± 12.6)% (Fig. 5h). As shown in Fig. 5i, treatment with CFZ-CaO_2@Lip induces maximal expression of cleaved PARP protein. These results indicate that the combination treatment by CFZ-CaO_2@Lip synergistically induces cell apoptosis.

3.5. Synergistic tumor growth inhibition by CFZ-CaO_2@Lip in vivo

For *in vivo* studies, the biocompatibility of CaO_2@Lip in mice was determined first. The BALB/c nude mice were injected with saline or CaO_2@Lip (20 mg kg^{-1} CaO_2) via the tail vein and sacrificed after 14 days. Blood samples were collected for detecting biochemical markers, including the activities of liver aminotransferases (aspartate aminotransferase (AST), alanine aminotransferase (ALT)) and the levels of kidney function indicators (blood urea nitrogen (BUN) and creatinine (CRE)). As shown in Fig. 6a, CaO_2@Lip does not affect the function of the liver or kidney. The major organs of the mice were collected for histochemical analysis by hematoxylin and eosin (H&E) staining. The result shows there is no harm to the organs after the treatment with CaO_2@Lip (Fig. 6b).

The biodistribution of the NPs plays a vital role in their *in vivo* therapeutic efficacy. The *in vivo* distribution of the CaO_2@Lip was studied in the mice bearing the tumors. U-87 MG-tumor bearing BALB/c nude mice were constructed by injecting U-87 MG cells subcutaneously into the backside flank. CaO_2@Lip was loaded a fluorescent dye DiR (1,1′-dioctadecyl-3,3,3′,3′-tetramethylindotricarbocyanine iodide), and DiR-loaded CaO_2@Lip (20 mg kg^{-1} CaO_2, 200 μg kg^{-1} DiR) was intravenously injected into the U-87 MG-tumor-bearing mice, and the main organs and tumors were harvested after 6 or 12 h. As shown in Fig. 7a, though the majority of CaO_2@Lip is retained in the liver and spleen, a high amount of CaO_2@Lip accumulates in the tumor due to the tumor passive targeting ability of CaO_2@Lip. A higher accumulation of CaO_2@Lip in the tumor was observed at 12 h compared to 6 h after injection.

In view of the ideal biocompatibility and passive tumor-targeting capability of CaO_2@Lip *in vivo*, along with the substantial synergistic inhibitory impact of CaO_2@Lip and CFZ@Lip on U-87 MG cell proliferation, *in vivo* antitumor effect of CFZ-CaO_2@Lip was subsequently investigated. When the tumor volume reached around 100 mm^3 (day 0),

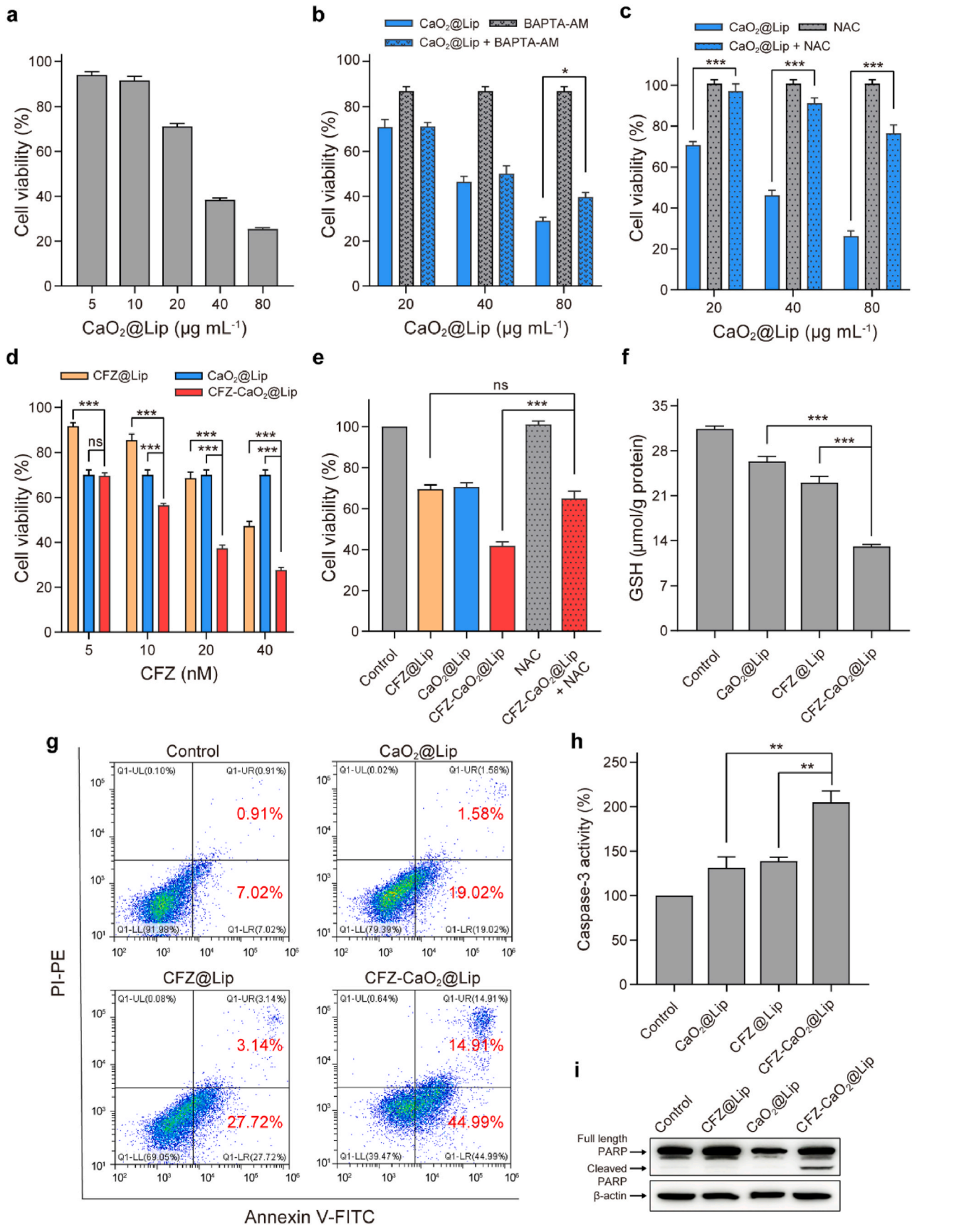

(caption on next page)

Fig. 5. Synergistic cytotoxicity induced by CFZ-CaO_2@Lip. (a) Viability of the cells after incubation with CaO_2@Lip (5−80 μg mL^{-1} CaO_2) for 48 h. (b) Viability of the cells after incubation with CaO_2@Lip (20−80 μg mL^{-1} CaO_2) in the presence or absence of BAPTA-AM (4 μM) for 48 h. (c) Viability of the cells after incubation with CaO_2@Lip (20−80 μg mL^{-1} CaO_2) in the presence or absence of NAC (2 mM) for 48 h. (d) Enhanced cytotoxicity of CFZ by CaO_2. The cells were treated with CFZ@Lip (5−40 nM CFZ), CaO_2@Lip (20 μg mL^{-1} CaO_2), or CFZ-CaO_2@Lip (5−40 nM CFZ, 20 μg mL^{-1} CaO_2) for 48 h. (e) Viability of the cells after incubation with CFZ@Lip (20 nM CFZ), CaO_2@Lip (20 μg mL^{-1} CaO_2), or CFZ-CaO_2@Lip (20 nM CFZ, 20 μg mL^{-1} CaO_2) in the presence or absence of NAC (2 mM) for 48 h. The cell viability was determined by MTT assay. (f) Reduced intracellular GSH content after the treatment with CFZ-CaO_2@Lip.The cells were treated with CFZ@Lip (20 nM CFZ), CaO_2@Lip (20 μg mL^{-1} CaO_2), or CFZ-CaO_2@Lip (20 nM CFZ, 20 μg mL^{-1} CaO_2) for 24 h. (g) Flow cytometry analysis of apoptosis after various treatments for 24 h. (h) Caspase-3 activity of the cells after various treatments for 24 h. (i) Western blotting analysis of PARP cleavage of the cells after the treatments for 24 h.

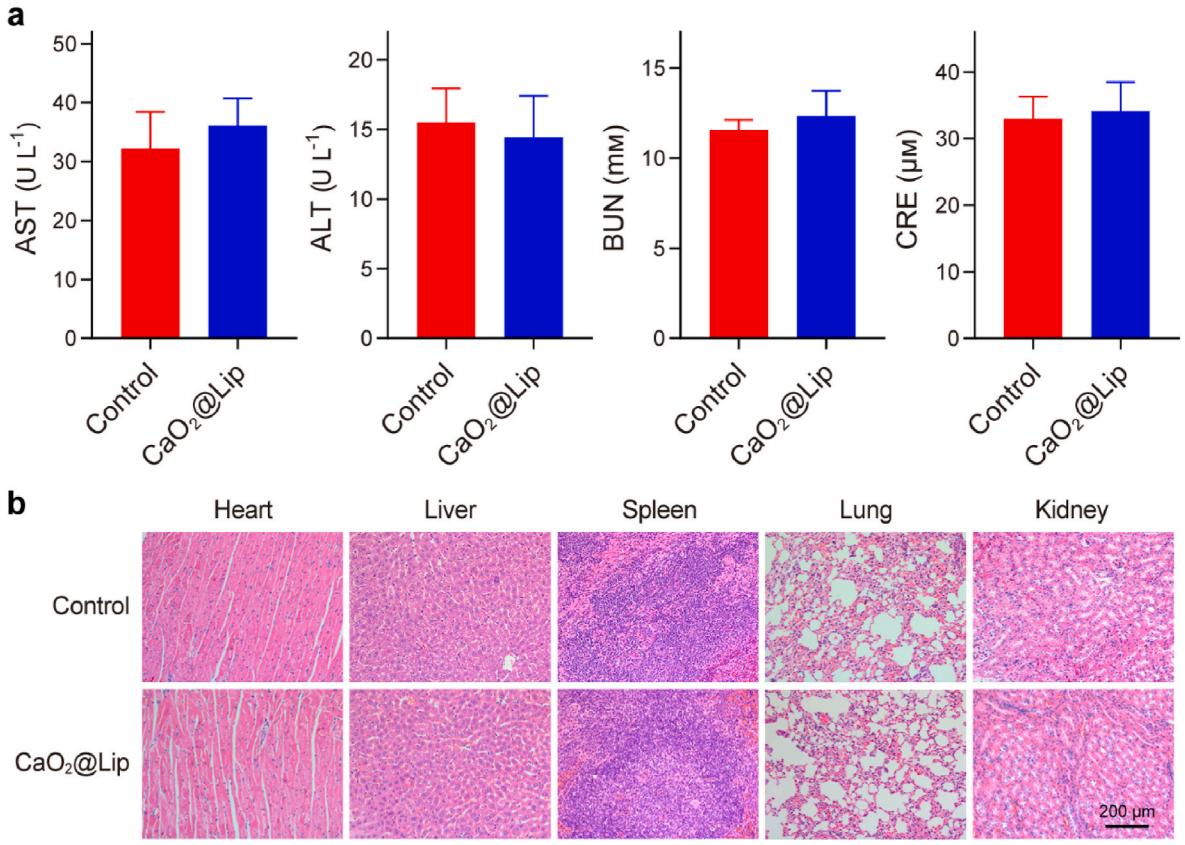

Fig. 6. *In vivo* biocompatibility study. (a) Blood biochemistry analysis of AST, ALT, BUN and CRE. (b) H&E staining of heart, liver, spleen, lung, and kidney of the mice. The mice were intravenously injected with saline or CaO_2@Lip (20 mg kg^{-1} CaO_2), and sacrificed after 14 days. The data shown represent the mean ± S.E.M., $n = 3$.

the mice were injected intravenously saline, CaO_2@Lip (20 mg kg^{-1} CaO_2), CFZ@Lip (2 mg kg^{-1} CFZ), or CFZ-CaO_2@Lip (20 mg kg^{-1} CaO_2, 2 mg kg^{-1} CFZ) on day 0, 2, 4, and 8. The body weight and tumor sizes of the mice were measured every two days until day 14. As shown in Fig. S8, there was no obvious change in the weight of mice. Compared with the control group, treatment with CaO_2@Lip or CFZ@Lip inhibits tumor growth to varying degrees, while treatment with CFZ-CaO_2@Lip shows the strongest tumor suppression (Fig. 7b and c). Correspondingly, the tumor weight data (Fig. 7d) also supports this result. Consistent with the *in vitro* results, CFZ-CaO_2@Lip induces the highest accumulation of ubiquitinated proteins from western blot analysis (Fig. 7e) and immunofluorescence staining of tumors (Fig. 7f).

H&E staining of tumor sections indicates that treatment with CaO_2@Lip or CFZ@Lip only results in minimal damage effects, whereas CFZ-CaO_2@Lip induces substantial tumor destruction, showing signs of nuclear pyknosis, karyolysis, and karyorrhexis (Fig. 7f). The CFZ-CaO_2@Lip group exhibits the highest ROS induction based on the DCFH-DA staining result (Fig. 7f), which correlates with the detection of GSH content in the tumors (Fig. S9). Ki67 and TUNEL staining were performed to evaluate the cell proliferation and apoptosis levels in the tumor, respectively. As expected, the minimal expression of Ki67 and maximal TUNEL-positive cells were observed in the tumors from the CFZ-CaO_2@Lip group (Fig. 7f), providing further evidence of the enhanced efficacy of CFZ by CaO_2.

The combination therapy with two or more anticancer drugs shows great potential in improving the therapeutic effect and broadening their indications [53,54]. Based on the crosstalk between proteasome inhibitors and oxidative stress, incorporation of CaO_2 was first proved to sensitize the anticancer efficacy of proteasome inhibitors.

4. Conclusions

In summary, liposomes were used to encapsulate CaO_2 NPs and proteasome inhibitor CFZ for combination therapy based on the crosstalk between proteasome inhibitors and oxidative stress. Under the acidic condition, CaO_2 can decompose and release both Ca^{2+} ions and H_2O_2. Low-dose CaO_2 synergistically enhances the anticancer effect of CFZ, which is attributed to the generation of ROS. The combination therapy synergistically induces the intracellular accumulation of ubiquitinated proteins and endoplasmic reticulum stress, subsequently leading to cell apoptosis. Taking advantage of passive tumor targeting ability of liposomes, the codelivery system delivers both CaO_2 and CFZ

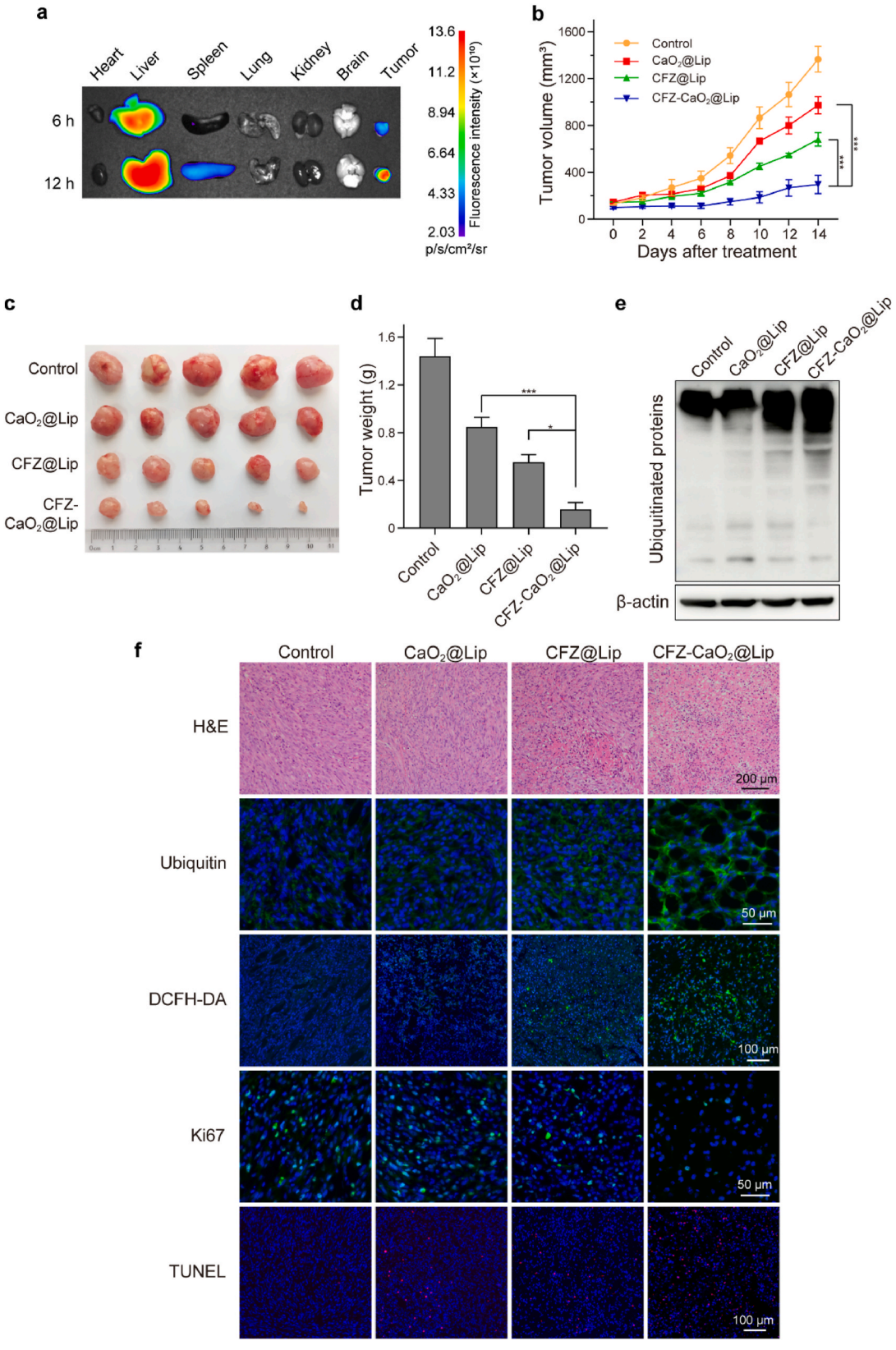

Fig. 7. *In vivo* anticancer effect of CFZ-CaO_2@Lip. (a) *In vivo* distribution of CaO_2@Lip. The DiR-loaded CaO_2@Lip (20 mg kg^{-1} CaO_2, 200 μg kg^{-1} DiR) was intravenously injected into U-87 MG-tumor bearing mice, and *ex vivo* fluorescence images of major organs and tumors were captured after 6 or 12 h. (b) Tumor volumes of the mice at various time points. The mice were intravenously injected with saline, CaO_2@Lip (20 mg kg^{-1} CaO_2), CFZ@Lip (2 mg kg^{-1} CFZ), or CFZ-CaO_2@Lip (20 mg kg^{-1} CaO_2, 2 mg kg^{-1} CFZ). (c) Photographs and (d) weights of tumors in different groups at the end points of the treatments. (e) Western blotting analysis of the expression of ubiquitinated proteins in the tumors. (f) H&E staining, immunofluorescence staining of ubiquitin (green), DCFH-DA (green), Ki67 (green) and TUNEL assay (red) of the tumor slices. The nuclei were stained with Hoechst 33342 (blue). The data shown represent the mean ± S.E.M., $n = 5$, $^{*}P < 0.05$, $^{***}P < 0.001$. (For interpretation of the references to colour in this figure legend, the reader is referred to the Web version of this article.)

to the tumor and exerts a superior antitumor effect in U-87 MG tumor-bearing mice compared with monotherapy. Taken together, CaO_2 shows great potential in sensitizing the proteasome inhibitors for solid tumor therapy.

CRediT authorship contribution statement

Dan Yin: Writing – original draft, Methodology, Investigation, Data curation, Conceptualization. **Xuan Wu:** Writing – original draft, Methodology, Investigation, Data curation. **Xu Chen:** Methodology, Investigation. **Jian-Li Chen:** Methodology, Investigation. **Xinyue Xia:** Methodology, Investigation. **Jianfang Wang:** Resources, Methodology, Investigation. **Xiuping Chen:** Resources, Methodology, Investigation. **Xiao-Ming Zhu:** Writing – review & editing, Supervision, Resources, Project administration, Funding acquisition, Conceptualization.

Declaration of competing interest

The authors declare that they have no known competing financial interests or personal relationships that could have appeared to influence the work reported in this paper.

Acknowledgements

This work was funded by Macau Science and Technology Development Fund (0035/2022/A1) and an open project of State Key Laboratory of Quality Research in Chinese Medicines funded by Macau Science and Technology Development Fund (Macau University of Science and Technology, 006/2023/SKL).

Appendix. ASupplementary data

Supplementary data to this article can be found online at https://doi.org/10.1016/j.mtbio.2025.101649.

Data availability

Data will be made available on request.

References

[1] G. Nalepa, M. Rolfe, J.W. Harper, Drug discovery in the ubiquitin-proteasome system, Nat. Rev. Drug Discov. 5 (2006) 596–613.
[2] J.A.M. Bard, E.A. Goodall, E.R. Greene, E. Jonsson, K.C. Dong, A. Martin, Structure and function of the 26S proteasome, Annu. Rev. Biochem. 87 (2018) 697–724.
[3] L.D. Fricker, Proteasome inhibitor drugs, Annu. Rev. Pharmacol. Toxicol. 60 (2020) 457–476.
[4] E.E. Manasanch, R.Z. Orlowski, Proteasome inhibitors in cancer therapy, Nat. Rev. Clin. Oncol. 14 (2017) 417–433.
[5] S. Kwon, K.B. Kim, Y. Yeo, W. Lee, Pharmacokinetic aspects of the clinically used proteasome inhibitor drugs and efforts toward nanoparticulate delivery systems, J. Pharm. Invest. 51 (2021) 483–502.
[6] X. Chen, X. Wu, L.Y. Li, X.-M. Zhu, Development of proteasome inhibitors for cancer therapy, Int. J. Drug Discov. Pharm. 3 (2024) 100004.
[7] J.D. Ashley, J.F. Stefanick, V.A. Schroeder, M.A. Suckow, N.J. Alves, R. Suzuki, S. Kikuchi, T. Hideshima, K.C. Anderson, T. Kiziltepe, B. Bilgicer, Liposomal carfilzomib nanoparticles effectively target multiple myeloma cells and demonstrate enhanced efficacy in vivo, J. Contr. Release 196 (2014) 113–121.
[8] J.E. Park, J. Park, Y. Jun, Y. Oh, G. Ryoo, Y.-S. Jeong, H.H. Gadalla, J.S. Min, J. H. Jo, M.G. Song, K.W. Kang, S.K. Bae, Y. Yeo, W. Lee, Expanding therapeutic utility of carfilzomib for breast cancer therapy by novel albumin-coated nanocrystal formulation, J. Contr. Release 302 (2019) 148–159.
[9] M.F. Zhang, L.W. Lu, M. Ying, H.T. Ruan, X.Y. Wang, H. Wang, Z.L. Chai, S. L. Wang, C.Y. Zhan, J. Pan, W.Y. Lu, Enhanced glioblastoma targeting ability of carfilzomib enabled by a DA7R-modified lipid nanodisk, Mol. Pharm. 15 (2018) 2437–2447.
[10] X. Wu, L. Wang, Y.-N. Xu, J.-L. Chen, K.Q. Luo, M.-H. Yuan, J. Li, G. Yuan, Z.-Y. Gu, X.-H. Jia, X.P. Chen, X.-M. Zhu, R.B. Jiang, Chemo-phototherapy with carfilzomib-encapsulated TiN nanoshells suppressing tumor growth and lymphatic metastasis, Small 18 (2022) 2200522.
[11] H.-Y. Wan, J.-L. Chen, X.Z. Zhu, L. Liu, J.F. Wang, X.-M. Zhu, Titania-coated gold nano-bipyramids for blocking autophagy flux and sensitizing cancer cells to proteasome inhibitor-induced death, Adv. Sci. 5 (2018) 1700585.
[12] X.Y. Chen, C.R. Shi, M.H. He, S.Q. Xiong, X.B. Xia, Endoplasmic reticulum stress: molecular mechanism and therapeutic targets, Signal Transduct. Targeted Ther. 8 (2023) 352.
[13] A. Görlach, K. Bertram, S. Hudecova, O. Krizanova, Calcium and ROS: a mutual interplay, Redox Biol. 6 (2015) 260–271.
[14] B.C. Lipchick, E.E. Fink, M.A. Nikiforov, Oxidative stress and proteasome inhibitors in multiple myeloma, Pharmacol. Res. 105 (2016) 210–215.
[15] L. Yin, T. Kufe, D. Avigan, D. Kufe, Targeting MUC1-C is synergistic with bortezomib in downregulating TIGAR and inducing ROS-mediated myeloma cell death, Blood 123 (2014) 2997–3006.
[16] X.Y. Pei, Y. Dai, S. Grant, Synergistic induction of oxidative injury and apoptosis in human multiple myeloma cells by the proteasome inhibitor bortezomib and histone deacetylase inhibitors, Clin. Cancer Res. 10 (2004) 3839–3852.
[17] R. Feng, A. Oton, M.Y. Mapara, G. Anderson, C. Belani, S. Lentzsch, The histone deacetylase inhibitor, PXD101, potentiates bortezomib-induced anti-multiple myeloma effect by induction of oxidative stress and DNA damage, Br. J. Haematol. 139 (2007) 385–397.
[18] B.Y. Niu, K.X. Liao, Y.X. Zhou, T. Wen, G.L. Quan, X. Pan, C.B. Wu, Application of glutathione depletion in cancer therapy: enhanced ROS-based therapy, Biomaterials 277 (2021) 121110.
[19] Q.B. Cui, J.-Q. Wang, Y.G. Assaraf, L. Ren, P. Gupta, L.Y. Wei, C.R. Ashby Jr., D.-H. Yang, Z.-S. Chen, Modulating ROS to overcome multidrug resistance in cancer, Drug Resist. Updates 41 (2018) 1–25.
[20] K.K. Starheim, T. Holien, K. Misund, I. Johansson, K.A. Baranowska, A.M. Sponaas, H. Hella, G. Buene, A. Waage, A. Sundan, G. Bjorkoy, Intracellular glutathione determines bortezomib cytotoxicity in multiple myeloma cells, Blood Cancer J. 6 (2016) e446.
[21] J. He, L.-H. Fu, C. Qi, J. Lin, P. Huang, Metal peroxides for cancer treatment, Bioact. Mater. 6 (2021) 2698–2710.
[22] H. Hu, L.D. Yu, X.Q. Qian, Y. Chen, B.D. Chen, Y.H. Li, Chemoreactive nanotherapeutics by metal peroxide based nanomedicine, Adv. Sci. 8 (2020) 2000494.
[23] S. Bai, Y.L. Lan, S.Y. Fu, H.W. Cheng, Z.X. Lu, G. Liu, Connecting calcium-based nanomaterials and cancer: from diagnosis to therapy, Nano-Micro Lett. 14 (2022) 145.
[24] Q. Qiu, J.X. Li, H. Ren, J.Y. Zhang, G.Q. Liu, R.Q. Yang, B.Y. Sun, C. Zhang, Y. M. Zhang, Zinc coordination lipid nanoparticles co-delivering calcium peroxide and chelating STING agonist for enhanced cancer metalloimmunotherapy, Small 20 (2024) 2402308.
[25] C. Jiang, W.X. Li, J. Yan, X.Y. Yu, Y.Z. Feng, B. Li, Y. Liu, Y.L. Dai, A robust ROS generation and ferroptotic lipid modulation nanosystem for mutual reinforcement of ferroptosis and cancer immunotherapy, Adv. Healthcare Mater. 13 (2024) 2401502.
[26] M. Zhang, R.X. Song, Y.Y. Liu, Z.G. Yi, X.F. Meng, J.W. Zhang, Z.M. Tang, Z. W. Yao, Y. Liu, X.G. Liu, W.B. Bu, Calcium-overload-mediated tumor therapy by calcium peroxide nanoparticles, Chem 5 (2019) 2171–2182.
[27] D.D. Guo, X.Y. Dai, K.W. Liu, Y.H. Liu, J.M. Wu, K. Wang, S.W. Jiang, F. Sun, L. J. Wang, B. Guo, D.Y. Yang, L.Q. Huang, A self-reinforcing nanoplatform for highly effective synergistic targeted combinatary calcium-overload and photodynamic therapy of cancer, Adv. Healthcare Mater. 12 (2023) 2202424.
[28] Y.J. Sheng, H. Nestbitt, B. Callan, M.A. Taylor, M. Love, A.P. McHale, J.F. Callan, Oxygen generating nanoparticles for improved photodynamic therapy of hypoxic tumours, J. Contr. Release 264 (2017) 333–340.
[29] F.Q. Shi, J. Chen, L.S. Yan, J. Yu, GSH-depleting and H_2O_2 self-supplying calcium peroxide-based nanoplatforms for efficient bacterial eradication via photothermal-enhanced chemodynamic therapy, ACS Appl. Mater. Interfaces 16 (2024) 69055–69070.
[30] X.W. Mo, N.M. Phan, T.L. Nguyen, J. Kim, H_2O_2 self-supplying CaO_2 nanoplatform induces Ca^{2+} overload combined with chemodynamic therapy to enhance cancer immunotherapy, ACS Appl. Mater. Interfaces 16 (2024) 58337–58345.
[31] Q.Q. Sun, B. Liu, R.X. Zhao, L.L. Feng, Z. Wang, S.M. Dong, Y.S. Dong, S.L. Gai, H. Ding, P.P. Yang, Calcium peroxide-based nanosystem with cancer microenvironment-activated capabilities for imaging guided combination therapy via mitochondrial Ca^{2+} overload and chemotherapy, ACS Appl. Mater. Interfaces 13 (2021) 44096–44107.
[32] C.C. He, S.S. Zhang, X.G. Liu, J.G. Wang, Y.M. Huang, A.X. Zhang, X.J. Zhang, CaO_2 nanomedicines: a review of their emerging roles in cancer therapy, Nanotechnology 34 (2023) 482002.
[33] K.M. Kortuem, A.K. Stewart, Carfilzomib, Blood 121 (2013) 893–897.
[34] A.Z. Wang, R. Langer, O.C. Farokhzad, Nanoparticle delivery of cancer drugs, Annu. Rev. Med. 63 (2012) 185–198.
[35] D.E. Large, R.G. Abdelmessih, E.A. Fink, D.T. Auguste, Liposome composition in drug delivery design, synthesis, characterization, and clinical application, Adv. Drug Deliv. Rev. 176 (2021) 113851.
[36] I. Canton, G. Battaglia, Endocytosis at the nanoscale, Chem. Soc. Rev. 41 (2012) 2718–2739.
[37] X.-M. Zhu, J. Yuan, K.C.-F. Leung, S.-F. Lee, K.W.Y. Sham, C.H.K. Cheng, D.W. T. Au, G.-J. Teng, A.T. Ahuja, Y.-X.J. Wang, Hollow superparamagnetic iron oxide nanoshells as a hydrophobic anticancer drug carrier: intracellular pH-dependent drug release and enhanced cytotoxicity, Nanoscale 4 (2012) 5744–5754.
[38] J.-L. Chen, H. Zhang, X.-Q. Huang, H.-Y. Wan, J. Li, X.-X. Fan, K.Q. Luo, J.H. Wang, X.-M. Zhu, J.F. Wang, Antiangiogenesis-combined photothermal therapy in the second near-infrared window at laser powers below the skin tolerance threshold, Nano-Micro Lett. 11 (2019) 93.
[39] J.-L. Chen, X.-H. Jia, X. Wu, M.-H. Yuan, X.Y. Xia, D. Yin, X. Chen, Z.-Y. Gu, J.-Z. Liu, L.-P. Bai, K.Q. Luo, J.F. Wang, X.-M. Zhu, Kidney-targeted antioxidant

salvianolic acid B nanoparticles restoring lysosome homeostasis for acute kidney injury therapy, Chem. Eng. J. 490 (2024) 151811.
[40] G.A. Collins, A.L. Goldberg, The logic of the 26S proteasome, Cell 169 (2017) 792–806.
[41] A.T. Nunes, C.M. Annunziata, Proteasome inhibitors: structure and function, Semin. Oncol. 44 (2017) 377–380.
[42] R. Bravo-Sagua, V. Parra, C. Lopez-Crisosto, P. Diaz, A.F. Quest, S. Lavandero, Calcium transport and signaling in mitochondria, Compr. Physiol. 7 (2017) 623–634.
[43] J.S. Bhatti, G.K. Bhatti, P.H. Reddy, Mitochondrial dysfunction and oxidative stress in metabolic disorders - a step towards mitochondria based therapeutic strategies, BBA-Mol. Basis. Dis. 1863 (2017) 1066–1077.
[44] J.L. Yao, H. Peng, Y. Qiu, S.X. Li, X.W. Xu, A.G. Wu, F. Yang, Nanoplatform-mediated calcium overload for cancer therapy, J. Mater. Chem. B 10 (2022) 1508–1519.
[45] A. Kodron, B.H. Mussulini, I. Pilecka, The ubiquitin-proteasome system and its crosstalk with mitochondria as therapeutic targets in medicine, Pharmacol. Res. 163 (2021) 105248.
[46] S.E. Logue, P. Cleary, S. Saveljeva, New directions in ER stress-induced cell death, Apoptosis 18 (2013) 537–546.
[47] A. Fribley, Q.H. Zeng, C.-Y. Wang, Proteasome inhibitor PS-341 induces apoptosis through induction of endoplasmic reticulum stress-reactive oxygen species in head and neck squamous cell carcinoma cells, Mol. Cell Biol. 24 (2004) 95.
[48] W.H. Park, S.H. Kim, MG132, a proteasome inhibitor, induces human pulmonary fibroblast cell death via increasing ROS levels and GSH depletion, Oncol. Rep. 27 (2012) 1284–1291.
[49] H.-Y. Chen, X.-Y. Ren, W.-H. Wang, Y.-X. Zhang, S.-F. Chen, B. Zhang, L.-X. Wang, Upregulated ROS production induced by the proteasome inhibitor MG-132 on XBP1 gene expression and cell apoptosis in Tca-8113 cells, Biomed. Pharmacother. 68 (2014) 709–713.
[50] P.S. Brookes, Y. Yoon, J.L. Robotham, M.W. Anders, S.-S. Sheu, Calcium, ATP, and ROS: a mitochondrial love-hate triangle, Am. J. Physiol. Cell Physiol. 287 (2004) C817–C833.
[51] G. Yuan, Y.N. Xu, X.P. Bai, W.M. Wang, X. Wu, J.L. Chen, J. Li, X.H. Jia, Z.Y. Gu, X. Zhang, W. Hu, J.F. Wang, Y. Liu, X.-M. Zhu, Autophagy-targeted calcium phosphate nanoparticles enable transarterial chemoembolization for enhanced cancer therapy, ACS Appl. Mater. Interfaces 15 (2023) 11431.
[52] X.M. Zhu, A. Fu, K.Q. Luo, A high-throughput fluorescence resonance energy transfer (FRET)-based endothelial cell apoptosis assay and its application for screening vascular disrupting agents, Biochem. Biophys. Res. Commun. 418 (2012) 641–646.
[53] J.-L. Chen, X. Wu, D. Yin, X.-H. Jia, X. Chen, Z.-Y. Gu, X.-M. Zhu, Autophagy inhibitors for cancer therapy: small molecules and nanomedicines, Pharmacol. Ther. 249 (2023) 108485.
[54] J.-L. Chen, X.-H. Jia, X.Y. Xia, X. Wu, Y.-N. Xu, G. Yuan, Z.-Y. Gu, K.Q. Luo, M.-H. Yuan, R.B. Jiang, J.F. Wang, X.-M. Zhu, Codelivery of vorinostat and chloroquine by autophagy-inhibitory hollow ZrO_2 nanoshells for synergistic combination chemotherapy, Chem. Eng. J. 471 (2023) 144740.